

Accelerating non-LTE synthesis and inversions with graph networks

A. VICENTE ARÉVALO ^{1,2}, A. ASENSIO RAMOS,¹ AND S. ESTEBAN POZUELO¹

¹*Instituto de Astrofísica de Canarias, C/Vía Láctea s/n, E-38205 La Laguna, Tenerife, Spain*

²*Departamento de Astrofísica, Universidad de La Laguna, E-38206 La Laguna, Tenerife, Spain*

ABSTRACT

The computational cost of fast non-LTE synthesis is one of the challenges that limits the development of 2D and 3D inversion codes. It also makes the interpretation of observations of lines formed in the chromosphere and transition region a slow and computationally costly process, which limits the inference of the physical properties on rather small fields of view. Having access to a fast way of computing the deviation from the LTE regime through the departure coefficients could largely alleviate this problem. We propose to build and train a graph network that quickly predicts the atomic level populations without solving the non-LTE problem. We find an optimal architecture for the graph network for predicting the departure coefficients of the levels of an atom from the physical conditions of a model atmosphere. A suitable dataset with a representative sample of potential model atmospheres is used for training. This dataset has been computed using existing non-LTE synthesis codes. The graph network has been integrated into existing synthesis and inversion codes for the particular case of Ca II. We demonstrate orders of magnitude gain in computing speed. We analyze the generalization capabilities of the graph network and demonstrate that it produces good predicted departure coefficients for unseen models. We implement this approach in `Haze12` and show how the inversions nicely compare with those obtained with standard non-LTE inversion codes. Our approximate method opens up the possibility of extracting physical information from the chromosphere on large fields-of-view with time evolution.

Keywords: Sun: atmosphere – Line: formation – Methods: data analysis – Sun: activity – Radiative transfer

1. INTRODUCTION

The physical parameters of astrophysical objects are routinely inferred by interpreting the observed (polarized) spectrum in a selection of spectral lines. To this end, a parametric physical model, which is assumed to be a good representation of the object under investigation, is proposed. This model defines the temperature, density, velocity and magnetic field at a predefined grid. This grid is three-dimensional in the general case, although two- and one-dimensional grids are often used as simplifications. Since the spectral lines are a consequence of transitions between pairs of energy levels in specific atoms and molecules, one also needs to specify a model atom/molecule. In the general case, the emergent polarization in a spectral line is obtained by simultaneously solving the vector radiative transfer equation (RTE) for the Stokes parameters and the statistical equilibrium equations (SEE) for the atomic level populations (Trujillo Bueno & Manso Sainz 1999). This

self-consistent solution of the RTE and SEE is known as the non-local thermodynamic equilibrium (non-LTE) problem. Since it is very difficult to solve, it is customary to make the simplifying assumption of neglecting atomic level polarization and work in what is commonly known as the Zeeman regime (Landi Degl’Innocenti & Landolfi 2004).

The non-LTE problem is nonlinear and nonlocal by nature. The nonlinearity appears because the propagation matrix (that describes the absorption and dispersion of radiation) and the emission vector that appear on the RTE depend on the atomic level populations. Likewise, the matrix elements of the SEE depend on the radiation field at each transition, which is obtained from the solution of the RTE. The nonlocality comes from the coupling between distant points in the grid induced by the RTE. Due to the nonlinear and nonlocal character of the non-LTE problem, iterative methods are required to find the self-consistent solution of the RTE and SEE equations. The practical majority of all methods in use

at the moment are based on variations of point iterations with specific accelerations (e.g., Hubeny & Mihas 2014), being the accelerated Λ -iteration (ALI) the most widespread among all. Although methods with faster convergence rates exist (see, e.g., Trujillo Bueno & Fabiani Bendicho 1995), ALI turns out to be ideal for its application to 3D problems.

The inference of the physical properties from the observation of spectral lines can be carried out by inverting the RTE and SEE equations. Although one can carry out this procedure by modifying by hand the proposed atmospheric model, it is much more efficient to rely on automatic methods. These methods, commonly known as ‘inversion codes’, iteratively modify a guess model until the difference between the radiation emerging from such model and the observations is small. The distance between the synthetic and the observed Stokes profiles is typically measured using the χ^2 metric. The majority of automatic methods use the Levenberg-Marquardt algorithm (a combination of a second order Newton method and a first order gradient descent method) to minimize the metric. To this end, they make use of response functions, i.e., the elements of the Jacobian matrix describing how the emergent Stokes profiles change when a perturbation is applied to the physical quantities. The response functions are difficult to obtain due to the non-linear and nonlocal character of the non-LTE problem, and arguably the most convenient way of computing them is through numerical evaluation using finite differences. As a consequence, each step of a non-LTE inversion requires many solutions of the full non-LTE forward problem (one for the synthesis and an additional set for the calculation of response functions using finite differences). It is apparent that a non-LTE inversion requires a significant amount of computation, even if, as shown by Milić & van Noort (2017), the non-LTE response functions can also be obtained efficiently using a semi-analytical approach.

The pioneering work of Socas-Navarro et al. (1998) was the first to consider the development of an inversion code for profiles in non-LTE. The code NICOLE was the first inversion scheme that could retrieve the stratification of physical properties from the interpretation of strong chromospheric spectral lines, which are commonly affected by non-LTE effects. Now, after more than two decades, we have two more codes at our disposal. Milić & van Noort (2018) developed SNAP1, a non-LTE inversion code based on the semi-analytical approach for the computation of the response function described in Milić & van Noort (2017). de la Cruz Rodríguez et al. (2019) developed the STockholm inversion Code (STiC), that upgrades the capabilities of pre-

vious non-LTE inversion codes by allowing the inversion of very strong lines that require partial redistribution (PRD) in angle and frequency. This is done in STiC by using the non-LTE synthesis code RH (Uitenbroek 2001) as a forward module. This code allows the user to invert strong lines like the Mg II multiplet, emerging from the upper chromosphere.

In contrast with the large computational requirements of non-LTE synthesis/inversion codes, the codes are much simpler when LTE conditions apply. LTE is reached whenever the source function is given by the Planck function or collisional processes are much more important than radiative processes. This assumption works, for instance, in many photospheric spectral lines, which are commonly used to analyze the deepest region of the solar photosphere. In this approximation, the propagation matrix and emission vector at each grid point depend only on local properties and can be expressed with closed analytical formulae (Sanchez Almeida 1992; Landi Degl’Innocenti & Landolfi 2004). This induces that the response functions can also be expressed in closed form. For this reason, inversion codes based on the LTE assumption were developed well before non-LTE inversion codes. Examples are the inversion codes SIR (Ruiz Cobo & del Toro Iniesta 1992) and SPINOR (Frutiger et al. 2000). In general, SIR can carry out tens of synthesis per second, including the evaluation of the response function. A typical non-LTE forward synthesis can require of the order of a few seconds to minutes, depending on the complexity of the problem. Therefore, a non-LTE iteration of an inversion code requires a factor 100 or more computing power than in the case of LTE.

Given this difference in speed, one would ideally like to have a non-LTE inversion code that performs as fast as an LTE code. This is motivated by the fact that current telescopes routinely produce spectro-polarimetric observations with fields of view (FOV) of the order of megapixels, in many cases with time evolution. The time consuming non-LTE inversion codes are routinely only applied to small subfields of the FOV and, even for this case, large supercomputers are required. From a theoretical point of view, a fast non-LTE inversion code could be obtained if one could have access, through an ‘‘instantaneous’’ computation (also known as oracle), to the so-called departure coefficients, the ratio between the populations in non-LTE and LTE. This is the motivation behind the recently developed DeSIRE code (Departure Coefficient aided Stokes Inversion based on Response functions; Ruiz Cobo et al. 2021, in press). DeSIRE uses RH to compute the departure coefficients solving the full non-LTE forward problem when the temper-

ature of the guess model has changed more than a certain threshold. In the rest of iterations, the inversion is performed with SIR assuming LTE with fixed departure coefficients.

In this contribution we propose a new type of approach, in the form of a trained graph network (GN; Battaglia et al. 2018). Other similar approaches based on machine learning are also under investigation (see Chappell & Pereira, submitted). The network uses the depth stratification of the physical conditions on an arbitrary 1D grid and produces the departure coefficients for a selection of atoms as output. The graph network is fast and differentiable, so it can be used in combination with an LTE inversion code to carry out non-LTE inversions much faster. This opens the possibility of quickly getting chromospheric information from large FOVs. We describe the architecture in the following, illustrating its capabilities in the forward and inverse problem. We open source the results in a public repository¹ so that they can be used by the community.

2. BYPASSING THE NON-LTE PROBLEM WITH GRAPH NETWORKS

2.1. Radiative transfer: a short summary

As described in the introduction, the standard multi-level radiative transfer problem requires the joint solution of the RTE equation, which describes the radiation field, and the SEE for the atomic/molecular level populations, which describe the excitation state (see, e.g., Mihalas 1978). We focus in this work on its solution in 1D plane-parallel atmospheres in the unpolarized case, since our main aim is to build fast inversion codes. Anyway, our approximation can be easily extended to the general 3D case including atomic level polarization (e.g., Jaume Bestard et al. 2021). We will investigate this in the future.

The basic physical properties of the atmosphere, (temperature, density, velocity, magnetic field, ...) are assumed to be known at a set of N_P discrete points along the atmosphere. The objective is to compute the populations of the N_L energy levels that are consistent with the radiation field within the stellar atmosphere. This radiation field has contributions from possible background sources and from the radiative transitions in the given atomic/molecular model.

The SEE are given by the following expressions, which are formally a linear system of equations in n_i , the populations of the energy levels:

$$\sum_{j \neq i} n_j P_{ji} - n_i \sum_{j \neq i} P_{ij} = 0. \quad (1)$$

In this equation, P_{ij} is the transition rate in s^{-1} between level i and j , any of which can be bound or free. Two different processes contribute to this transition rate. Collisions between the model atom/molecule and external abundant species induce collisional transitions between levels i and j with a rate given by C_{ij} . Additionally, radiative processes, denoted as R_{ij} , produce transitions between energy levels following certain selection rules. The total transition rate is then the sum of both terms $P_{ij} = C_{ij} + R_{ij}$.

The collisional rates C_{ij} only depend on the local physical conditions. On the other hand, the radiative rates R_{ij} depend on the radiation field, which is a non-local quantity. For bound-bound transitions, we have:

$$\begin{aligned} R_{ij} &= B_{ij} \bar{J}_{ij} & i < j \\ R_{ji} &= B_{ji} \bar{J}_{ji} + A_{ji} & i < j, \end{aligned} \quad (2)$$

where B_{ij} and B_{ji} are the Einstein coefficients for stimulated emission and absorption, respectively, A_{ji} is the Einstein coefficient for spontaneous emission and \bar{J}_{ij} (\bar{J}_{ji}) is the mean frequency-averaged intensity weighted by the absorption (emission) profile:

$$\begin{aligned} \bar{J}_{ij} &= \frac{1}{4\pi} \int d\Omega \int d\nu \phi_{ij}(\nu, \Omega) I_{\nu\Omega} \\ \bar{J}_{ji} &= \frac{1}{4\pi} \int d\Omega \int d\nu \psi_{ij}(\nu, \Omega) I_{\nu\Omega}. \end{aligned} \quad (3)$$

The symbols ϕ_{ij} and ψ_{ij} stand for the normalized line absorption and emission profiles, respectively. In the complete frequency redistribution (CRD) approximation, $\bar{J}_{ij} = \bar{J}_{ji}$ is fulfilled because the line emission and absorption profiles are the same. $I_{\nu\Omega}$ is the specific intensity at frequency ν and direction Ω . The explicit directional dependence in the line profiles account for directional Doppler shifts due to macroscopic velocity fields in the medium. The integration has to be carried out for the full 4π solid angle subtended by the sphere and for the frequency range of the transition. Similar expressions are found for bound-free transitions but with the mean intensity averaged over the photoionization cross-section, $\alpha_{ij}(\nu)$ (see, e.g. Rutten 2003).

The specific intensity is governed by the RT equation:

$$\frac{d}{ds} I_{\nu\Omega} = \chi_{\nu\Omega} (S_{\nu\Omega} - I_{\nu\Omega}). \quad (4)$$

which describes the variation of the specific intensity at frequency ν along a ray of direction Ω . $\chi_{\nu\Omega}$ and $S_{\nu\Omega}$ are the opacity and the source function, respectively, and s is the geometrical distance along the ray (see, e.g., Mihalas 1978). The opacity describes how the photons are absorbed when being transported in the atmosphere,

¹ https://github.com/andreuva/graphnet_nlte

while the source function describes the generation of new photons in the atmosphere. The opacity and the source function have three main contributions. The first one is coming from continuum transitions of background species. We assume that this opacity can be obtained locally from the physical conditions at each spatial point in the grid. This contribution includes, for example, the free-free and bound-free absorption processes in hydrogen, the background molecular species which are treated in LTE, opacity due to metals, absorption due to interstellar dust, etc. The second contribution is from the atomic/molecular model bound-bound transitions, that can be computed from the population of the upper and lower levels. Finally, the last contribution is due to continuum transitions in the atomic/molecular model.

Following Rybicki & Hummer (1992) (see also Uitenbroek 2001; Osborne & Milić 2021), we write the emissivity (ϵ) and the opacity (χ) for a general transition between an upper level j and a lower level i as:

$$\begin{aligned}\chi_{ij}(\nu, \Omega) &= n_j U_{ji} \\ \epsilon_{ij}(\nu, \Omega) &= n_i V_{ji} - n_j V_{ji}\end{aligned}\quad (5)$$

The positive term in the opacity accounts for the direct absorption from the lower to the upper level and the negative term accounts for the stimulated emission from the upper to the lower level. The total emissivity and opacity for a given frequency is obtained by adding together all sources. The expression for the U and V terms are the following:

$$U_{ji} = \begin{cases} \frac{h\nu}{4\pi} A_{ji} \psi_{ij}(\nu, \Omega), & \text{bound - bound} \\ n_e \Phi_{ij}(T) \left(\frac{2h\nu^3}{c^2} \right) e^{-h\nu/kT} \alpha_{ij}(\nu), & \text{bound - free,} \end{cases} \quad (6)$$

$$V_{ij} = \begin{cases} \frac{h\nu}{4\pi} B_{ij} \phi_{ij}(\nu, \Omega), & \text{bound - bound} \\ n_e \Phi_{ij}(T) e^{-h\nu/kT} \alpha_{ij}(\nu), & \text{bound - free,} \end{cases} \quad (7)$$

$$V_{ji} = \begin{cases} \frac{h\nu}{4\pi} B_{ji} \psi_{ij}(\nu, \Omega), & \text{bound - bound} \\ \alpha_{ij}(\nu), & \text{bound - free,} \end{cases} \quad (8)$$

where $n_e \Phi_{ij}(T)$ is given by the Saha-Boltzmann equation (e.g., Mihalas 1978), with n_e the electron number density.

The source function can be obtained as the ratio

$$S_{ij\nu, \Omega} = \frac{\epsilon_{ij}(\nu, \Omega)}{\chi_{ij}(\nu, \Omega)}. \quad (9)$$

For our purpose, the previous equations can be more conveniently rewritten in terms of the departure coefficient which, for any arbitrary level k , is given by

$$b_k = \frac{n_k}{n_k^*}, \quad (10)$$

where n_k^* is the population of level k in LTE. This population can be easily obtained by applying the Saha-Boltzmann equation, which only depends on local quantities. For instance, the opacity for a bound-bound transition can be rewritten as

$$\chi_{\nu\Omega} = \frac{h\nu}{4\pi} b_l n_l^* \phi_{\nu\Omega} \left(1 - \frac{b_u}{b_l} e^{-h\nu/kT} \right), \quad (11)$$

and the equivalent line source function as

$$S_{\nu\Omega} = \frac{2h\nu_0^3}{c^2} \frac{1}{\frac{b_l}{b_u} e^{h\nu/kT} - 1} \frac{\psi_{\nu\Omega}}{\phi_{\nu\Omega}}, \quad (12)$$

where ν_0 is the central wavelength of the transition.

2.2. Graph networks

Our objective is to define and train a neural network that can quickly produce the departure coefficients for all the levels of the atom of interest at all points in the grid. The architecture of the neural network has to fulfill some properties to be of practical use. First, it needs to be fast. This is trivially fulfilled by almost any architecture when compared with the computing time needed to solve the non-LTE problem. Second, it needs to be flexible, so that one can apply it to arbitrary grids and not to a predefined one. Third, it needs to take into account that the non-LTE problem is nonlocal and nonlinear. Therefore, the possible correlation between the information from far apart grid points needs to be properly considered. An architecture that fulfills all these properties is the recently developed graph networks of Battaglia et al. (2018).

The fundamental idea consists in viewing the atmospheric grid in the atmosphere (1D, 2D or 3D) as the connected graph $G = (V, E)$, where V is the set of grid points (also known as nodes or vertices) and E is the set of edges connecting the grid points. This allows one to apply graph networks to an arbitrary number of grid points, placed at arbitrary locations in the atmosphere (so it is easy to work with non-cartesian atmospheres in multiple dimensions). Each node represents the set of relevant physical properties $\mathbf{p}_i \in V$ at each location of the atmosphere. Each edge $\mathbf{e}_{ij} \in E$ connects the two nodes i (sender) and j (receiver), and describes relevant inter-node properties.

A schematic representation of all the processing involved in a graph network, as defined by Battaglia et al. (2018), is shown in Fig. 1. The physical representation displays how a one-dimensional model atmosphere is transformed into a connected graph. Nodes encode physical properties p_i and edges encode internode information. The second step is to project the properties of

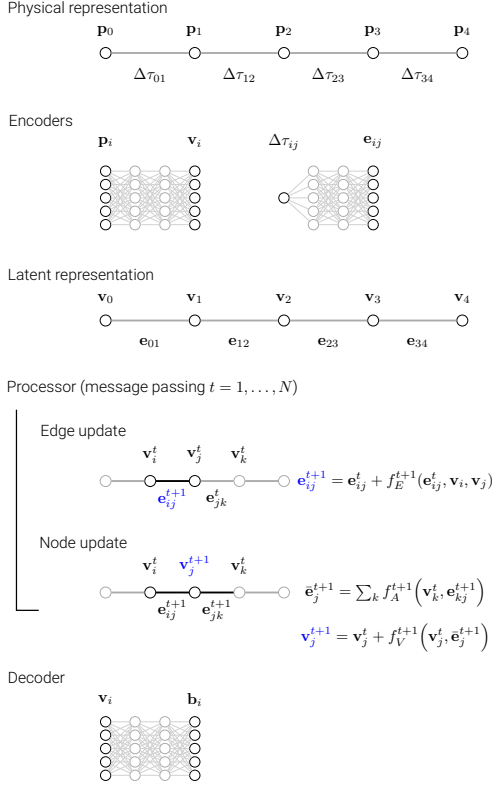


Figure 1. Schematic representation of the graph networks used to predict the departure coefficients. The quantities marked in blue in the processor phase are the ones being updated.

the nodes and edges to a latent space of higher dimension with the aid of two fully connected neural encoders. This projection largely increases the information encoding capabilities of the graph network. For simplicity, we use the same dimensionality for both variables. The resulting graph is shown in the latent representation, where nodes and edges are labeled with their corresponding latent variables.

As described by Battaglia et al. (2018), the core of the graph network occurs in the processor part, made of N consecutive message passing processes. Each message passing consists of updating the latent information contained in all edges and then in all nodes. At iteration t , the edge update phase uses a fully connected neural network, f_E^{t+1} , to modify the information encoded in the edge. The neural network accepts as input the concatenation of the edge and the nodes that are connected by the edge, and produces a modified output using an additional residual connection (He et al. 2016):

$$\mathbf{e}_{ij}^{t+1} = \mathbf{e}_{ij}^t + f_E^{t+1}(\mathbf{e}_{ij}^t, \mathbf{v}_i^t, \mathbf{v}_j^t). \quad (13)$$

This very same neural network is applied to all edges (they can be done in parallel) but it is different for each iteration of the message passing.

The node update step modifies the node latent information by using a couple of fully connected networks, f_A^{t+1} and f_V^{t+1} . The first one is used to compute an effective edge information for each node. In general, we use

$$\bar{\mathbf{e}}_j^{t+1} = \sum_k f_A^{t+1}(\mathbf{v}_k^t, \mathbf{e}_{kj}^{t+1}), \quad (14)$$

where the summation is carried out over all edges k for which the node j is a receiver (in practice we use averaging instead of summation to reduce gradient explosion when backpropagating during training). A simpler form of this equation, which also gives good results (Pfaff et al. 2020; Sánchez-González et al. 2020), is to simply average the value of the edges directly connecting other nodes to node j . In this case, spatial invariance is introduced as an additional inductive bias, something that can be of interest in case one wants this symmetry to be conserved (see Battaglia et al. 2018). Finally, the value of the node is updated by using:

$$\mathbf{v}_j^{t+1} = f_V^{t+1}(\mathbf{v}_j^t, \bar{\mathbf{e}}_j^{t+1}). \quad (15)$$

Note that the encoding, decoding, node and edge update functions are fully connected neural networks (FCNN), which take as inputs the physical quantities, node and/or edge values and connect them to the desired output. Also note that the nodes at the extremes of the graph have only one edge.

These FCNN use a combination of simple building blocks, containing a series of learnable weights and biases, to approximate a function or process through a carefully designed architecture (see, e.g., Chollet 2017). The basic building block is the following:

$$\mathbf{a}^L = \sigma(\mathbf{W}\mathbf{a}^{L-1} + \mathbf{b}^{L-1}), \quad (16)$$

where \mathbf{a}^{L-1} and \mathbf{a}^L are the input from a previous layer and the output vector of the building block at layer L , respectively. The building block applies a matrix of weights, \mathbf{W} , to the input and adds a bias, \mathbf{b}^{L-1} , and then passes the result through a nonlinear activation function σ . The dimensions of \mathbf{a}^{L-1} and \mathbf{a}^L can be different depending on the size of the layers $L-1$ and L respectively, so in general we have: $\mathbf{a}^L \in \mathbb{R}^n$, $\mathbf{a}^{L-1} \in \mathbb{R}^m$, $\mathbf{b}^{L-1} \in \mathbb{R}^n$, $\mathbf{W} \in \mathbb{R}^{n \times m}$.

Message passing is fundamental to connect the information in very distant nodes in the graph. Given that all updates are local (and can therefore be carried out in parallel), a simple reasoning shows that $\sim N_p$ iterations are needed to connect the information in all nodes in

our simple graph topology. This number could be potentially reduced if a more complex connectivity is used but its analysis is left for a future study.

A final decoder projects the values of the latent space in the nodes to the desired output. In our case, we predict the departure coefficients for the N_L levels of interest. This projection is again done in parallel for all nodes in the graph.

2.3. Specifics of GN for the non-LTE problem

After a trial and error process, we decided to encode in the nodes the temperature, T , in K, optical depth of the grid point (measured at 500 nm with $\tau_{500} = \int \chi_{500} ds$), electron number density, n_e , in m^{-3} , microturbulent velocity, v_{mic} , in m s^{-1} , and line of sight velocity, v_{LOS} , also in m s^{-1} . We use the logarithm of all the quantities, except for the velocities, to deal with the large variability. The selection of these five variables has given very good results as shown in this paper, but nothing fundamentally limits taking into account more information in case of necessity. This would be the case of the presence of, for instance, strong magnetic fields, that would have an important impact on the RTE and SEE (see Sec. 3.1).

In our case, for the edges, we only use the optical distance measured at 500 nm between the nodes as the encoded information. With this selection, $\mathbf{e}_{ij} = -\mathbf{e}_{ji}$, but the formalism is general and can seamlessly deal with asymmetric edge properties. For simplicity, we only consider edges that connect consecutive nodes. The results shown in this paper demonstrate that this is a good election, although we will explore more complex graphs structures in the future, where each node is connected to the nearest k neighbors.

We point out that there is a certain degree of overlap on the information encoded in the nodes and edges because the optical depth is encoded in both. However, given the enormous variability in the optical depth axes for all the models that we consider for training and validation, we found that encoding its absolute value in the nodes gave better generalization properties. We defer for the future potential simplifications of the node encoding to reduce the overlap.

3. TRAINING

3.1. Building the training set

The graph network is trained with results from calculations performed with the Lightweaver framework (Osborne & Milić 2021). Given the time consuming solution of the non-LTE forward problem, the ease of use of the Lightweaver framework facilitates the deployment of the generation of the training set in a parallel machine. Al-

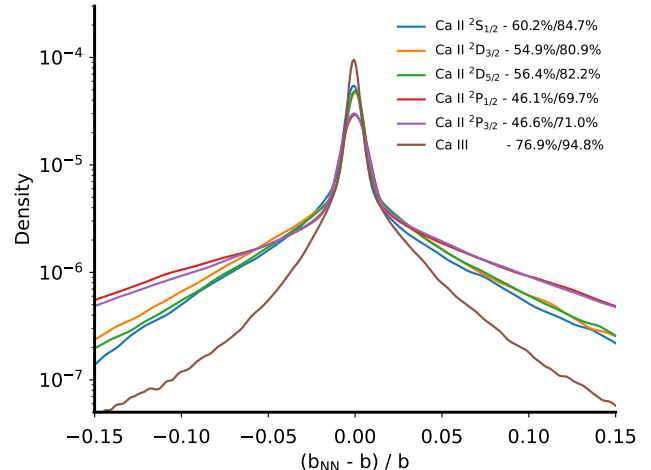


Figure 2. Gaussian kernel density estimation of the relative error between the correct departure coefficient and the one predicted by our neural approach for all energy levels considered in the Ca II model. The legend shows the percentage of cases for which b/b_{NN} are in the intervals $[-0.01, 0.01]$ and $[-0.05, 0.05]$, respectively.

though the method is general, we focus here on results for Ca II whose lines are widely used to infer the properties of the chromosphere. The Ca II infrared triplet is routinely used to extract quantitative information from the lower- to mid-chromosphere, given that plenty of observations are available. In this work we make use of observations performed with the CRISP instrument (Scharmer et al. 2008) mounted on the Swedish 1-m Solar Telescope (SST; Scharmer et al. 2003; Scharmer 2006).

The model atom that we used is part of the Lightweaver distribution. We use a simple atomic model that contains the five bounded energy levels $4s^2S_{1/2}$, $4p^2P_{1/2}$, $4p^2P_{3/2}$, $3d^2D_{3/2}$ and $3d^2D_{5/2}$, responsible for the Ca II infrared triplet and the H & K lines in the blue part of the spectrum. We also add the Ca III ground term to take into account all bound-free ionization transitions. The lines of the infrared triplet are treated in CRD, while the H & K lines are treated in PRD. It is worth noticing that the CRD and PRD cases have different complexity levels. However, due to the large approximation capacity of the GN we do not need to adapt the basic procedure, except perhaps increasing the complexity of the GN by using more complex neural networks in cases in which the approximation error is unacceptable large.

All calculations are made under the field-free simplifying approximation for the sake of clarity, but it can be lifted if needed without fundamentally affecting the procedure. This approximation assumes that the solution of the SEE is unaffected by the presence of Zeeman

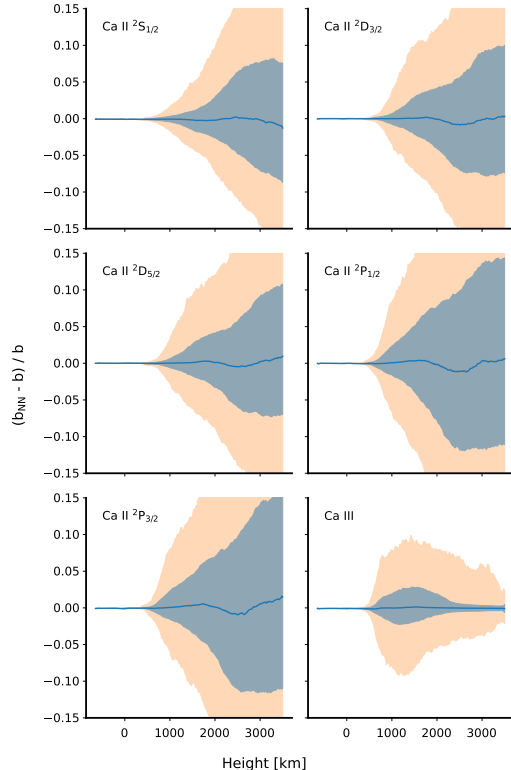


Figure 3. Geometrical height distribution of the relative error between the correct departure coefficient and the one predicted with the GN for all the Ca II and Ca III atomic energy levels. The median value is indicated with a solid blue line, while the shaded blue and orange regions indicate the 68% and 95% probability, respectively.

splitting in the energy levels (Rees 1969). If the magnetic field is very large, one should add its effect on the SEE. In this case, apart from increasing the computation time for the generation of the database, one would probably need to add the magnetic field strength (and potentially its orientation) as a new parameter in the nodes of the GN.

With the sake of producing a GN that generalizes properly to new unseen models, we put some emphasis on generating a database of atmospheric models with significant excursions on all the physical properties. To this end, we use the semi-empirical FAL-A, FAL-C, FAL-F and FAL-XCO models (Fontenla et al. 1993) as baselines and add perturbations in the temperature, microturbulent and line-of-sight velocities. We use signed Gaussian random perturbations with a standard deviation of 2500 K for the temperature, a relative perturbation of 20% for the microturbulent velocity and 2.5 km s^{-1} for the line-of-sight velocity. All these perturbations are realized at nodes located at $\log \tau_{500} = -5, -4, -3, -2, -1, 0$. Prior to adding them to the underlying model, these perturbations are ade-

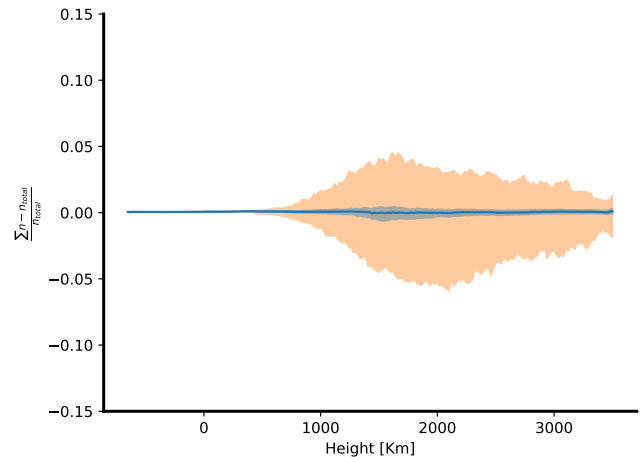


Figure 4. Height distribution of the relative error between the sum of the populations inferred with the computed departure coefficients and the true sum of populations for all the Ca II and Ca III atomic energy levels. The median value is indicated with a solid blue line, while the shaded blue and orange regions indicate the 68% and 95% probability, respectively.

quately interpolated and smoothed to avoid very strong gradients that might compromise the convergence of the non-LTE problem. Since we have perturbed the temperature, the electron density of the model is not anymore consistent. For this reason, the electron pressure is computed for these models assuming hydrostatic equilibrium. To this set of randomized models, we add models extracted from the snapshot at $t = 3850 \text{ s}$ of the enhanced network simulation of Carlsson et al. (2016), computed with the Bifrost code (Gudiksen et al. 2011). The microturbulent velocity of these models is set to zero. A total of 70 000 models have been produced in three datasets. One dataset contains 50 000 of those models and are actually used during training, while the remaining 20 000 are used as validation and test sets to tune the hyperparameters and check for over-fitting and generalization.

The full non-LTE problem for Ca II is solved in each model atmosphere using Lightweaver using the MALI method with full preconditioning, similarly to RH. The process is run in a distributed machine with 60 cores and takes ~ 16 hours.

3.2. Optimization

There are a few hyperparameters that need to be defined a priori. The most important ones are the size of the latent space used by the encoders (i.e., the dimension of vectors v_i and e_{ij}), the number of message passing iterations and the specific architecture of all fully connected neural networks. We carried out a system-

atic parametric study and found some values that seem optimal. The size of the latent space is set to 64. All neural networks, i.e., the encoder, the decoder, f_V^t , f_A^t and f_E^t , contain two hidden layers of size 64 with an ELU (Clevert et al. 2016) activation function. Concerning the number of message passing steps, we find a significant increase in precision when more message passing steps are used, albeit with a significant increase in memory consumption. For this reason, and because the improvement slows down significantly with more steps, we find a balance by setting the number of message passing steps to 100.

The neural networks are coded in PyTorch (Paszke et al. 2019), using the PyTorch Geometric package (Fey & Lenssen 2019) for neural networks in graphs. We use the Adam optimizer (Kingma & Ba 2014) with a learning rate of 10^{-4} , which is annealed at each epoch using a cosine rule. The training is done by optimizing the mean squared error (MSE) between the predicted and computed departure coefficients in logarithmic scale. We use a logarithm scale because the departure coefficients are spread over several orders of magnitude. The number of total trainable parameters is ~ 5.5 M. We train for 400 epochs on an NVIDIA GeForce RTX 2080Ti, for a total of 52 h. Due to GPU memory constraints, the batch size was limited to 32-64.

4. VALIDATION

4.1. Departure coefficients

Once trained, we checked the generalization properties of the GN, which is fundamental in any approach based on machine learning. To this end, we utilize the snapshot at $t = 5300$ s from the Bifrost simulation. This snapshot is extracted 24 min after the one used for training. This time is a few times larger than the typical lifetime of a granule, so the new snapshot can be considered to be sufficiently uncorrelated with the one used for training. We solve the non-LTE problem in all columns of this new snapshot and compare the results with those of the neural prediction. After training, our baseline GN displays an average MSE loss computed over this test dataset of 10^{-4} . Though this points out to a good generalization capabilities of the GN, we analyze the results in more detail.

Figure 2 displays the probability distribution of the relative difference between the computed departure coefficient and the one predicted by the GN for all the atomic levels considered in the Ca II model in a random subsample of 5 000 pixels. The legend also displays the percentage of pixels in the simulation with a relative error below 1% and 5%, respectively. The distributions are very peaky (note that they are displayed in loga-

rithmic scale), with a relatively Gaussian central core and extended wings. These distributions figures clearly show the generalization capabilities of the GN, giving predicted departure coefficients of significant precision in unseen data.

This distribution is affected by the fact that the departure coefficients in the deeper zones of the atmosphere are very close to unity, which our GN predicts very well. Only a small fraction of all available heights really contribute to the formation of the Ca II lines. In order to better display this behavior, Fig. 3 shows the distribution of relative errors as a function of geometrical height in the 3D snapshot. The solid blue line shows the median, while the shaded blue and orange areas denote the $\pm 68\%$ and $\pm 95\%$ percentiles. It is clear that our prediction for the deeper regions is always very good since all levels are in LTE. The quality of the prediction decreases with height, reaching relative differences larger than 15% in the upper part of the snapshot. These heights correspond to the base of the corona or the upper part of the transition region, depending the selected pixel, but they are not important for the formation of any of the Ca II lines. For the regions where the lines are formed, we find relative errors that are safely below 5% with 68% probability.

It is important to point out that, in cases in which very precise departure coefficients are needed or to reduce the probability of failure during the iterative solution, one can utilize the GN approximate values as initial populations for solving the non-LTE problem. We have checked that, using the ALI method, this amounts to a reduction in the number of iterations needed for convergence of a factor between 2 and 4. Although relevant, the gain in computing time is not specially important because ALI methods become slower when getting closer to the solution.

4.2. Density conservation

The atomic level populations computed with a non-LTE code fulfill, by construction, that their sum is equal to the total number density of the specific atomic species. For the specific case of our Ca II-Ca III atomic model:

$$\sum_i n_i = \sum_i b_i n_i^* = n_{\text{CaII}} + n_{\text{CaIII}}, \quad (17)$$

where we assume that the abundance of Ca I is negligible. Since the GN is used to predict b_i , we need to check at which level the previous condition is fulfilled. Figure 4 shows the relative error in the normalization of the populations that we incur when using the GN. Most of the predictions give abundances that are consistent

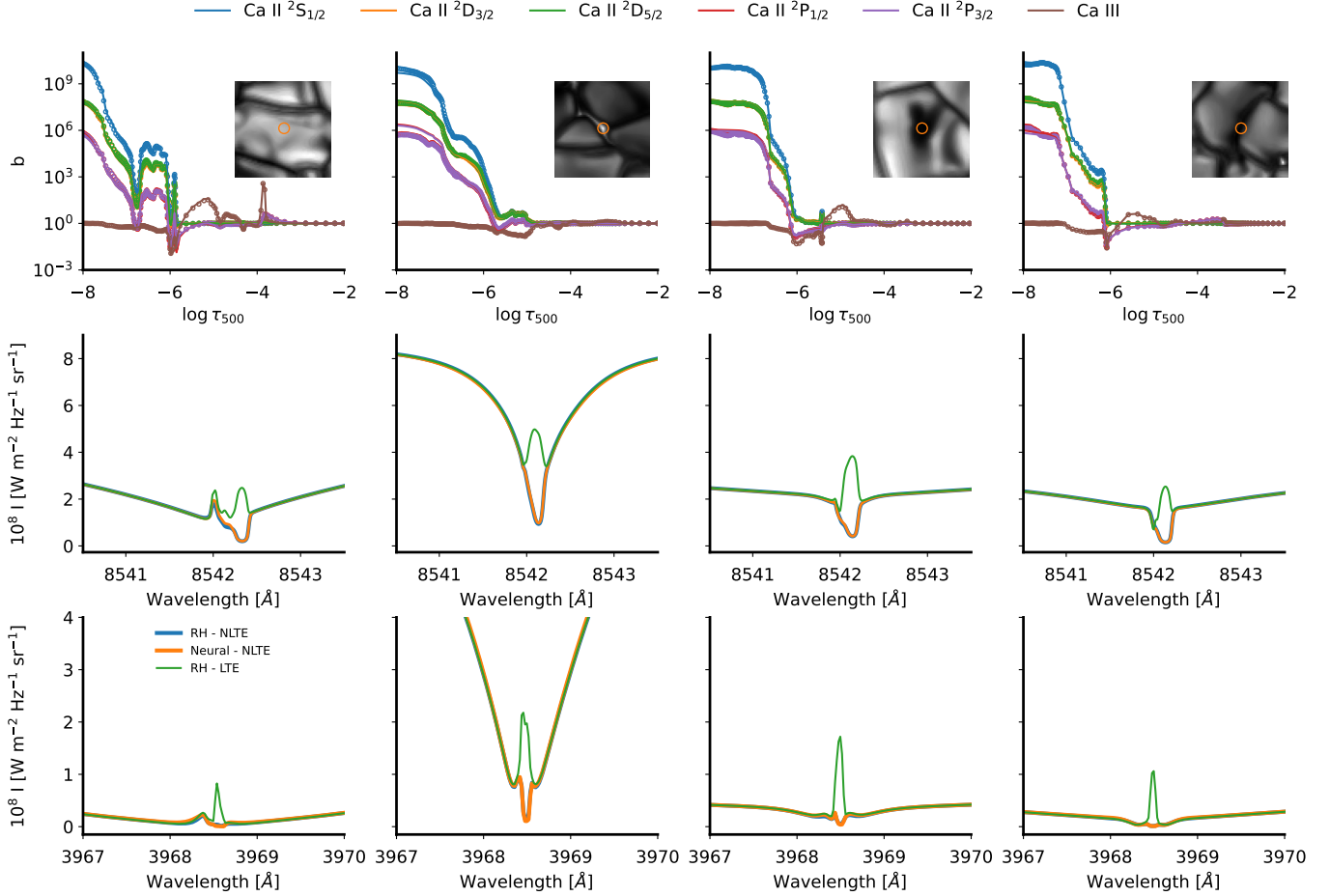


Figure 5. Upper panels: original (dotted) and approximated (solid) stratification of the departure coefficients with τ_{500} for all relevant levels of the Ca II model atom on a few selected pixels from the Bifrost simulation snapshot shown in the right panel (we display the temperature map at $\tau_{500} = 1$). Middle panels: synthetic spectral line of the widely used Ca II line at 854.2 nm using the original departure coefficients (blue) and the approximate ones (orange). For comparison, we also show the profile in LTE conditions in green. Lower panels: synthetic spectral line of the Ca II K line at 396.8 nm, computed in PRD.

throughout the whole atmosphere. We find deviations clearly below 2% with 68% probability, and below 5% with 98% probability.

4.3. Line profiles

Although the GN produces a good approximation to the departure coefficient, the definitive check requires the synthesis of the line profile. According to Eqs. (11) and (12), errors in the predicted departure coefficients can be partially compensated. This is the case of the source function, where only the ratio between departure coefficients appear, while a good prediction of the departure coefficient for the lower level is fundamental for a good estimation of the opacity. In other words, one can still produce a good approximate line profile even if the approximate departure coefficients are not in excellent agreement with the correct one. To this end, we synthesized the line profiles for the Ca II K (in PRD) and 8542

Å (in CRD) lines at four representative locations in the 3D snapshot. We show the results in Fig. 5. The upper row displays the calculated departure coefficients (dotted) for all levels of the Ca II model, together with the neural prediction. The precise pixel in the simulation can be seen in the inset. Given the remarkable similarities on the departure coefficients, the level populations obtained from these approximate departure coefficients produce synthetic spectral lines at $\mu = 1$ (with μ the heliocentric angle) in non-LTE that almost overlap with the full calculation, as can be seen in the middle (for the 8542 Å line) and lower (for the K line) rows of Fig. 5. Note that the lines are asymmetric due to the presence of strong velocity gradients with height in the selected pixels. For comparison, we show in green the line obtained in LTE, which is trivially obtained by setting $b_i = 1$.

With our GN, the prediction of the departure coefficients takes around 25 ms in a NVIDIA GeForce RTX

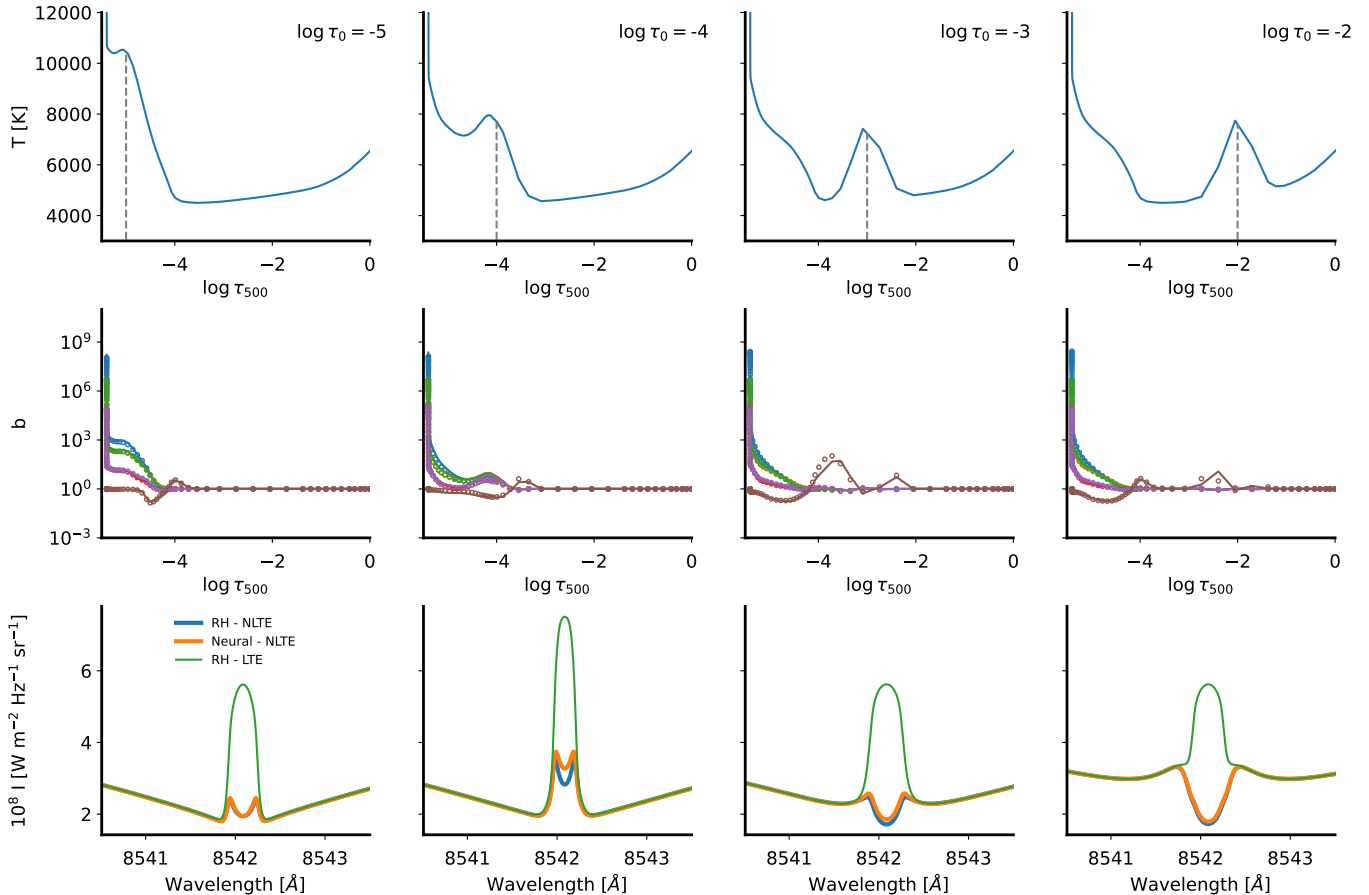


Figure 6. Generalization checks of a FAL-C model atmosphere to which a strong local increase in the temperature is added at different heights. The upper row shows the temperature stratification. The middle row shows the original (dotted) and approximated (solid) departure coefficients. The lower row shows the synthetic lines using the correct departure coefficients (blue) and the approximated ones (orange), together with the profile in LTE (green).

2080Ti, when done in serial. This includes all the input/output operations required to load the input on the GPU memory and unload the results to the CPU memory. Exploiting the parallelization properties of GPUs, a batch of roughly 50 such models can be fit into typical GPU memory at once, producing similar computing times. On the other hand, the computation of the departure coefficients with Lightweaver can take 20 s in an Intel Xeon-6130 CPU @ 2.10 GHz. As a consequence, our approach produces a speedup factor of 10^3 with a negligible impact on precision. Arguably, larger speedups can be obtained with smarter graph constructions that require less message passing steps.

As an additional test, we carry out the experiment of computing the emergent line profile in the 8542 Å line when a strong localized heating occurs at different positions on the atmosphere. These models were not favored by the procedure followed for the generation of the training set, so they are a good generalization test. Additionally, they represent situations that surely hap-

pen in the solar atmosphere. The results are summarized in Fig. 6. As shown in the upper panel of the figure, the proposed bump has Gaussian shape with an amplitude of 3000 K and a full width at half maximum of 0.7 in $\log \tau_{500}$ units. It is added to the temperature stratification of the FAL-C model. The central location of the heating is marked by the dashed grey line. The central panel shows the correct (dotted) and approximate (solid) departure coefficients, with the same color code as that used in Fig. 5. Finally, the lower panel displays the emergent intensity profiles at $\mu = 1$. The line profiles are very similar to the correct ones, even though some differences exist in the central core. The differences are larger when the perturbations occur on the line formation region. These differences should then be taken as representative of the uncertainty in the line profile introduced by the GN.

5. INVERSIONS

5.1. Response functions

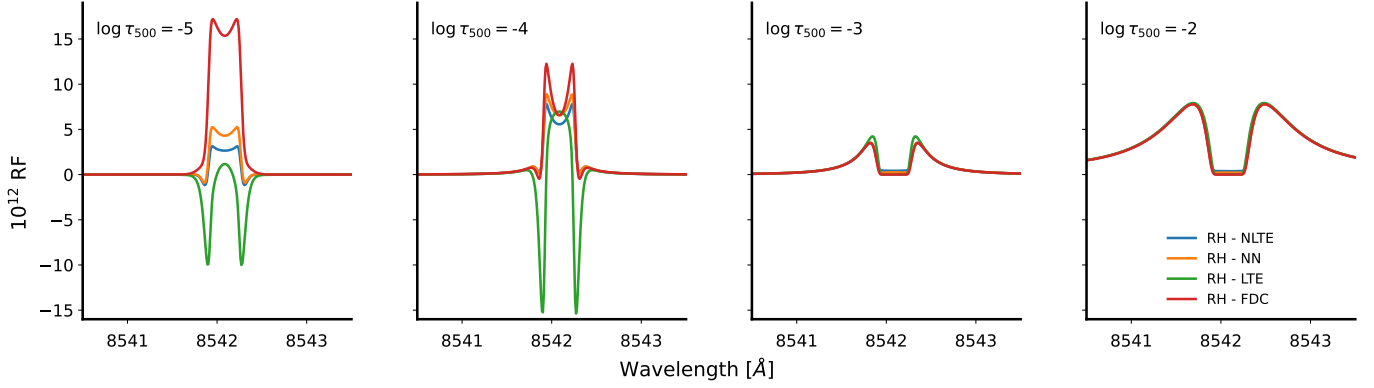


Figure 7. Response functions, in units of 10^{-12} , at four different optical depth heights for the FAL-C model atmosphere. The response functions are computed numerically using the full non-LTE calculation (blue), the approximate GN solution (orange), in LTE (green) and in the fixed departure coefficient case (red).

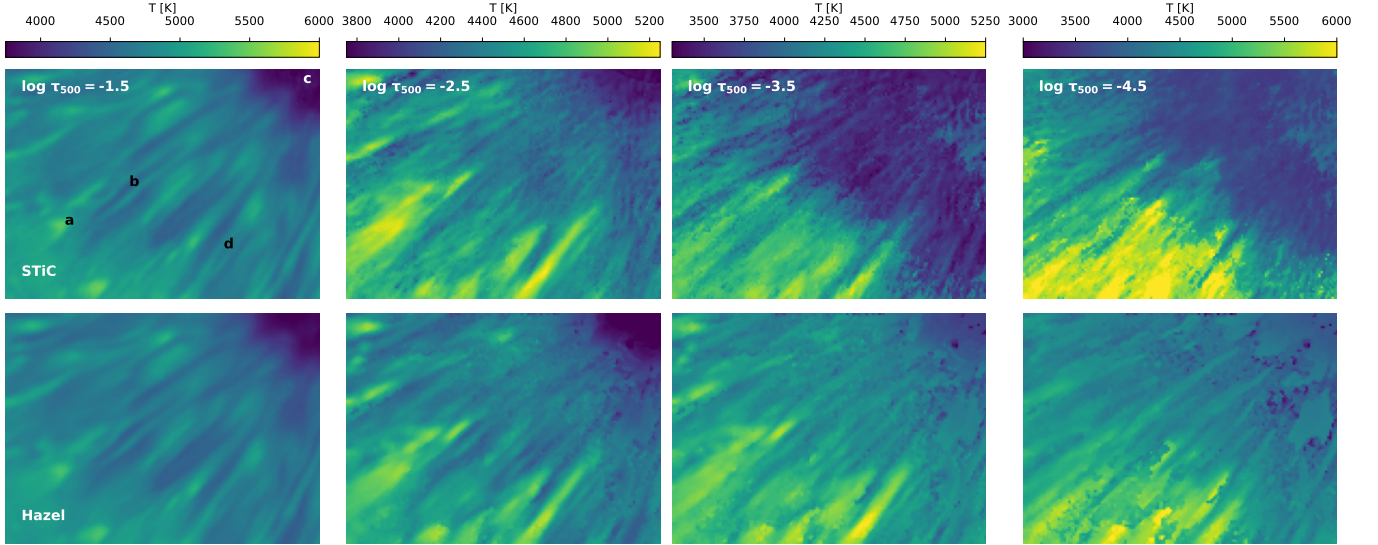


Figure 8. Temperature stratification at different optical depth surfaces obtained with STiC (upper panels) and Haze12 (lower panel). The letters refer to the position of the profiles displayed in Fig. 10.

As already mentioned, response functions are the derivative of the emergent line profile with respect to the physical conditions in the atmosphere. Having such precise Jacobian turns out to be crucial for the development of a fast inversion code. We demonstrate with Fig. 7 that the GN approximation gives good approximations to the response functions. The response functions are computed in the FAL-C model on 6 nodes equispaced in $\log \tau_{500}$. The temperature of each node is perturbed by a small amount (± 25 K) and centered finite differences are used to compute the response functions. Four cases are considered in Fig. 7. The first one (blue) is the correct non-LTE response function computed with Lightweaver. The second one (orange) uses the GN to compute the departure coefficients. The third case (green) assumes that all departure coefficients are unity

(LTE). The fourth case (red) assumes that the departure coefficients are not affected by the perturbation and are given by those of the unperturbed atmosphere. This is also known as the fixed departure coefficients (FDC) case (Socas-Navarro et al. 1998). The FDC approximation clearly overestimates the response of the line to the temperature at the higher layers, as shown by Milić & van Noort (2017). The response function is very similar to the correct one at lower layers for all approximations. Our results clearly demonstrate that adding the dependence of the GN on the physical conditions during the computation of the numerical derivatives leads to a very good approximation of the response functions. This anticipates the very good convergence results that we show in the following.

5.2. Inversion results

As discussed in the introduction, the GN serves as the perfect machinery to carry out very fast non-LTE inversions. We implemented it into the `Haze12` inversion code (Asensio Ramos et al. 2008) for the inversion of observations of the Ca II 8542 Å line. `Haze12` utilizes the SIR machinery for the synthesis of lines in LTE. In order to synthesize the line in non-LTE, the opacity and source function computed with SIR are modified according to Eqs. (11) and (12) in the CRD approximation, with the departure coefficients computed with the GN. Note that using the CRD approximation for the synthesis of the Ca II 8542 Å line is a good approximation because the GN returns the departure coefficients with the Ca II H & K lines computed in PRD.

Since `Haze12` computes response functions using finite differences, and the GN is differentiable by construction, the influence of the departure coefficients are seamlessly included. This means that one is effectively working in the non-fixed departure coefficient case. Although not strictly necessary, we checked that departure coefficients do not need to be recomputed at every iteration. We empirically found good results by recomputing them only when the maximum change in the temperature during the inversion procedure is larger than 50-100 K.

There is a significant computing time advantage of the non-LTE option of `Haze12` with respect to any other non-LTE inversion code. Since inversion codes are routinely run in parallel supercomputers, the GN cannot be run in a dedicated GPU, in general. Therefore, we need to resort to the less efficient CPU computation, which is roughly 10 times slower than a dedicated GPU. We assume ~ 250 ms and ~ 20 s for the computation of the departure coefficients using a GN or the ALI iterative scheme, respectively. Consequently, our method is approximately a factor $f = (t + 20)/(t + 0.2)$ faster, where t is the time required for common tasks like computing hydrostatic equilibrium or solving the radiative transfer equation. Typical values are found to be $t < 0.1$ s, so that $f > 67$. In other words, one can carry out non-LTE inversions only slightly slower than LTE inversions.

The data that we invert consist of a scan from a time sequence of full-Stokes measurements of a penumbral region taken at high spatial resolution with CRISP in the Ca II 8542 Å line. The data were obtained on July, 27th 2020, between 08:35:09 and 08:52:48 UT. At that time, the hosting sunspot was located at a heliocentric distance of 25.8 degrees. During the observation, the Ca II 8542 Å line was sampled at 15 wavelength positions in the range $[-1.755, 1.755]$ Å, with steps of 65 mÅ close to the line center, and wider in the wings. Each scan was completed every 21 s. We acquired 12 accumulations

per wavelength step and modulation state. The FOV of the observations is of about $55'' \times 55''$, and the pixel size is $0''.057$, which gives a total of 965×965 pixels. Due to the computational limitations of standard non-LTE inversions, we only analyze a small subfield of 147×107 pixels, equivalent to $8.3'' \times 6.1''$. We carried out the data reduction using the SSTRED pipeline (de la Cruz Rodríguez et al. 2015; Löfdahl et al. 2021), and images were restored using the Multi-Object Multi-Frame Blind Deconvolution technique (MOMFBD; Löfdahl 2002; van Noort et al. 2005). The inversions are carried out both with STiC and `Haze12`, taking into account the transmission profile of the CRISP instrument.

Given the differences between `Haze12` and STiC in terms of all the microphysics and the inversion procedure, we do not expect both inversions to give exactly the same results. Since our interest here is to investigate how the GN works in non-LTE inversions, we put the emphasis on Stokes I and the temperature. The STiC inversions are done in three cycles. The first two cycles consider one every 10th pixel. We characterize the configuration of each cycle with the vector $(n_T, n_v, n_{vmic}, n_B)$, which gives the number of nodes in temperature, line-of-sight velocity, microturbulent velocity and magnetic field components. The configuration for the first two cycles is (7,2,1,2) and (7,3,3,3). After the second cycle, we interpolate the results for all pixels and carry out a final cycle with (7,3,3,3). In `Haze12` we simply invert every pixel from scratch using two cycles with (3,1,1,0) and (5,2,2,1) using FAL-C as a reference model. The average inversion time per pixel with `Haze12` in an AMD Epyc 7452 CPU is 9.8 s.

The temperature maps at four different optical depth surfaces are shown in Fig. 8. The spatial appearance is remarkably similar between both inversion codes, with clear chromospheric structures appearing for layers above $\log \tau_{500} \leq -2$. The photospheric temperatures ($\log \tau_{500} \geq -2.5$) are essentially indistinguishable, not only in their aspect but also in the amplitude of the temperature. The results in higher layers ($\log \tau_{500} = -4.5$) are slightly different. The information encoded in the profiles for such heights is reduced and the results depend on the specific assumptions of the model and the details of the inversion. This is not surprising since the CRISP data is undersampled, which surely produces a loss of sensitivity around the central core, which is sampling heights in the range $\log \tau_{500} = [-5, -4]$. For heights above these, one should not put any emphasis on existing differences among codes because the lines do not have any sensitivity (Quintero Noda et al. 2016). Adding more lines that help sample these regions is the

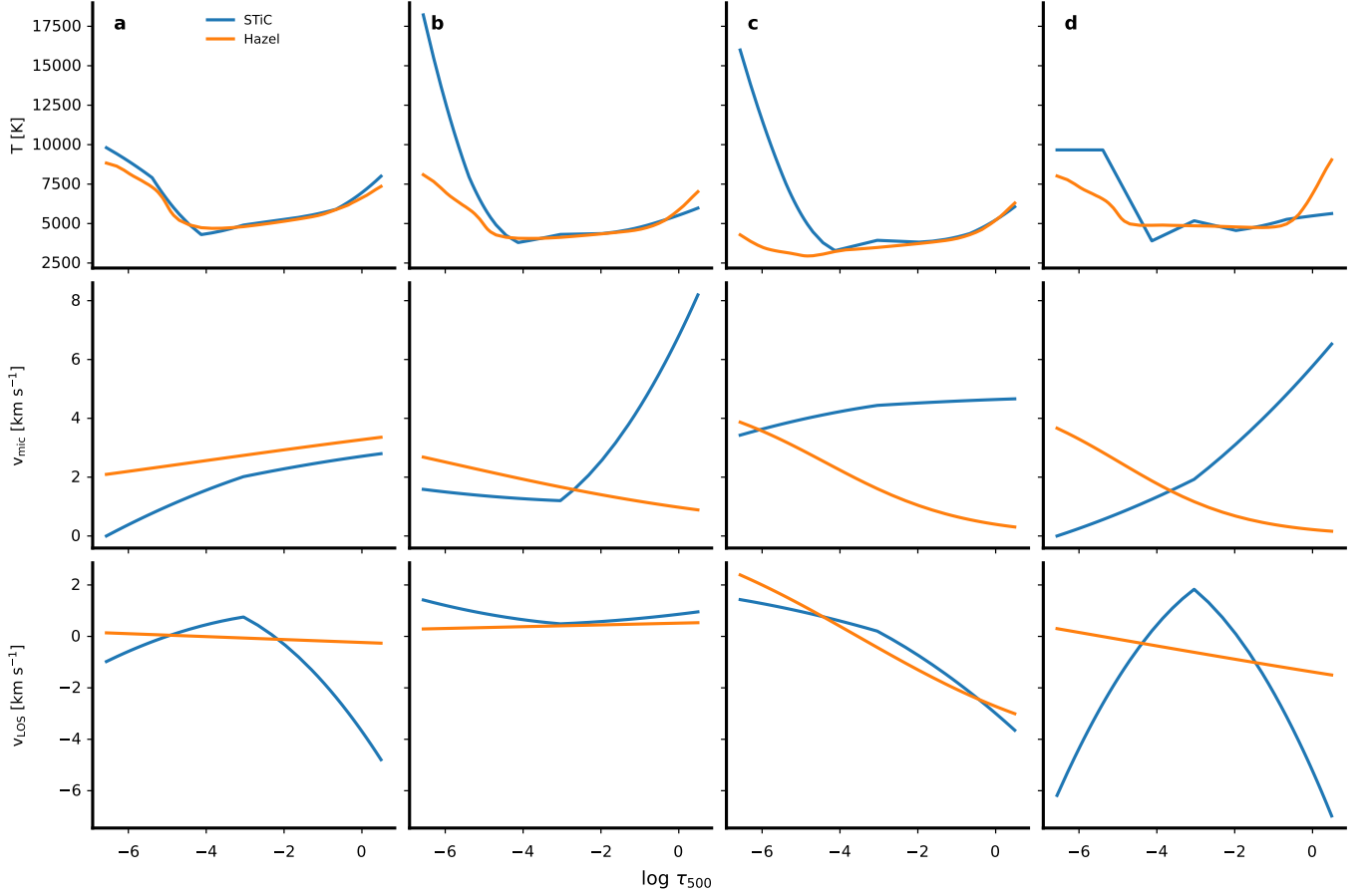


Figure 9. Depth stratification of the temperature (upper panel), microturbulent velocity (middle panel) and line-of-sight velocity (lower panel) for the pixels shown in Fig. 8 inferred with STiC (blue) and Haze12 (orange).

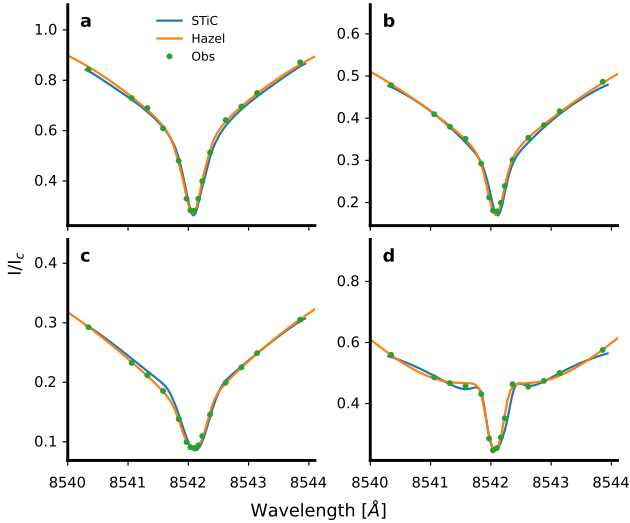


Figure 10. Observed Stokes I profiles (green dots), together with the fits produced by STiC and Haze12. These profiles correspond to the pixel locations found in Fig. 8.

only way to produce a more constrained solution (da Silva Santos et al. 2018).

For a more in-depth analysis of the difference between the results of the two inversion codes, we show in Fig. 9 the depth stratifications of the temperature, microturbulent velocity and line-of-sight velocity for the four pixels marked in Fig. 8. Haze12 is based on the strategy proposed by Ruiz Cobo & del Toro Iniesta (1992) of using a reference model as baseline. This model is iteratively modified at the nodes. It is obvious that the results of Haze12 still display some memory from the FAL-C model used as reference. Meanwhile, STiC directly inverts the value of the physical properties at the nodes. Anyway, the similarities between both results are obvious in the regions where there is sensitivity. The results are not expected to be exactly the same due to the differences between the two synthesis codes, the different parameterization of the solution and how the iterative inversion proceeds. In the regions without sensitivity, both results might diverge but have negligible impact on the emergent profile. As discussed above, one should

not focus on the differences in these regions of negligible sensitivity for the Ca II 8542 Å line.

Despite these differences in the stratification of the physical properties, the Stokes I profiles are correctly reproduced with the two codes. Figure 10 displays the Stokes I profiles for the four selected points. The green dots show the observed profile, with the orange and blue curves displaying the `Haze12` and `STiC` synthetic profile in the inferred model, respectively. Both fits display a similar quality.

6. CONCLUSIONS AND FUTURE WORK

We have shown that non-LTE problems can be solved very fast using a graph network for predicting the value of the departure coefficients from the physical conditions. The forward evaluation of the GN is orders of magnitude faster than the solution of the non-LTE problem. This greatly accelerates the synthesis, opening up the possibility of quickly calculating synthetic profiles of strong lines with non-LTE effects. In cases in which the approximate departure coefficients are not precise enough, one can use them as initialization for the full non-LTE problem. This leads to a significant reduction on the computing time because fewer ALI iterations (between half and one-fourth) are needed.

Arguably the most straightforward application of our GN is to accelerate non-LTE inversion codes. As a proof of concept, we have implemented the neural approach in the `Haze12` inversion code, so that it can use the LTE machinery of `SIR` to carry out non-LTE inversions of Ca II lines. We find that the computing time is reduced by a significant factor when compared with classical approaches to non-LTE inversions. Given all the uncertainties of a non-LTE inversion procedure (observational noise, lack of flexibility of the model, ambiguities, uncertainties in the atomic data,...), our approximation turns out to be very competitive. The fact that we introduce a small error on the estimation of the departure coefficients is only an extra component of this inherent uncertainty.

We demonstrated the fast inversions with data from the `CRISP` instrument showing a good comparison with the results obtained with `STiC`. We point out that the implementation in `Haze12` can only be used for lines for which the CRD approximation is valid because it uses `SIR` internally. This is a good option for the lines of the infrared triplet of Ca II. If lines need to be computed taking into account PRD effects, one needs to use codes like `RH`. An acceleration of the inversion is still possible because the departure coefficients can be computed with the GN and no MALI iteration is needed at all. We plan

to add this option to `Haze12` in the near future through the use of the `Lightweaver` framework.

Although we have particularized all calculations to the prediction of the departure coefficients in 1D plane-parallel cases, graph networks are general. They can be seamlessly applied to higher dimensions and to arbitrary topologies and for the prediction of other quantities. An obvious extension of this work is to compute departure coefficients or mean intensities in 3D snapshots, taking into account horizontal radiative transfer effects. This would require the solution of the 3D non-LTE problem, something that can be done with codes like `RH` or `MULTI3D` (Leenaarts & Carlsson 2009). The main difficulty resides on the computational effort to find a sufficiently large training set.

We focus in this work on the computation of the departure coefficients for the energy levels of the Ca II model atom. However, the method is general and can deal with any atomic system or even combinations of them. Training such a GN could be of potential interest to deal with recent multi-instrument inversions that use lines from Ca II with `CRISP` and `CHROMIS` on the `SST`, Mg II and Si IV with the `Interface Region Imaging Spectrograph` (`IRIS`; De Pontieu et al. 2014) and `Atacama Large Millimeter Array` (`ALMA`) continua to map the chromosphere and the transition region (e.g., Vissers et al. 2019; da Silva Santos et al. 2020).

Despite the good results, some caveats are in order. First, our results are based on a pre-computed training set. If any of the assumptions used during the computation of this set need to be changed, the trained GN is of no utility and a new training needs to be carried out. Second, although we have checked that the GN generalizes correctly to some unseen models, the training set is obviously missing models that describe energetic events, like those occurring in flares. We anticipate that model atmospheres computed with the `RADYN` code (Carlsson & Stein 1992, 1997) can also be included in the training set to aid in the generalization properties for this kind of energetic events. This would probably require the inclusion of other physical quantities as new parameters of the nodes. Additionally, the assumption of hydrostatic equilibrium can be lifted in these dynamic models. Likewise, the `Bifrost` 3D snapshot corresponds to a relatively quiet region, while active regions are not part of the training set. Whenever a suitable MHD simulation of an active region including realistic chromospheres and transition regions is available, one can also add them to the training set. Finally, we need to explore improvements to the architecture and on the selection of hyperparameters to produce a GN with lower generalization error in upper atmospheric layers.

We thank C. Quintero Noda for providing the 3D snapshots used in this work. We thank J. de la Cruz Rodríguez, M. J. Martínez González, T. del Pino Alemán, C. Quintero Noda, and J. Štěpán for helpful suggestions to improve the paper. We acknowledge financial support from the Spanish Ministerio de Ciencia, Innovación y Universidades through project PGC2018-102108-B-I00 and FEDER funds. This work was partly supported by the European Research Council (ERC) under the European Union’s Horizon 2020 research and innovation programme (ERC Advanced Grant agreement No. 742265). This paper uses data acquired at the Swedish 1-m Solar Telescope, operated on the island of La Palma by the Institute for Solar Physics of Stockholm University in the Spanish Observatorio del Roque de los Muchachos of the Instituto de Astrofísica de Canarias. The Institute for Solar Physics is supported by a grant for research infrastructures of national importance from the Swedish Research Council (registration number 2017-00625). The authors thankfully acknowledge the technical expertise and assistance provided by the Spanish Supercomputing Network (Red Española de Supercomputación), as well as the computer resources used: the LaPalma Supercomputer, located at the Instituto de Astrofísica de Canarias. This research has made use of NASA’s Astrophysics Data System Bibliographic Services. We acknowledge the community effort devoted to the development of the following open-source packages that were used in this work: `numpy` (numpy.org, Harris et al. 2020), `matplotlib` (matplotlib.org, Hunter 2007), `PyTorch` (pytorch.org, Paszke et al. 2019).

REFERENCES

- Asensio Ramos, A., Trujillo Bueno, J., & Landi Degl’Innocenti, E. 2008, *ApJ*, 683, 542
- Battaglia, P. W., Hamrick, J. B., Bapst, V., et al. 2018, arXiv e-prints, arXiv:1806.01261.
<https://arxiv.org/abs/1806.01261>
- Carlsson, M., Hansteen, V. H., Gudiksen, B. V., Leenaarts, J., & De Pontieu, B. 2016, *A&A*, 585, A4,
doi: [10.1051/0004-6361/201527226](https://doi.org/10.1051/0004-6361/201527226)
- Carlsson, M., & Stein, R. F. 1992, *ApJL*, 397, L59,
doi: [10.1086/186544](https://doi.org/10.1086/186544)
- . 1997, *ApJ*, 481, 500, doi: [10.1086/304043](https://doi.org/10.1086/304043)
- Chollet, F. 2017, *Deep Learning with Python* (Manning)
- Clevert, D., Unterthiner, T., & Hochreiter, S. 2016, in 4th International Conference on Learning Representations, ICLR 2016, San Juan, Puerto Rico, May 2-4, 2016, Conference Track Proceedings, ed. Y. Bengio & Y. LeCun. <http://arxiv.org/abs/1511.07289>
- da Silva Santos, J. M., de la Cruz Rodríguez, J., & Leenaarts, J. 2018, *A&A*, 620, A124,
doi: [10.1051/0004-6361/201833664](https://doi.org/10.1051/0004-6361/201833664)
- da Silva Santos, J. M., de la Cruz Rodríguez, J., Leenaarts, J., et al. 2020, *A&A*, 634, A56,
doi: [10.1051/0004-6361/201937117](https://doi.org/10.1051/0004-6361/201937117)
- de la Cruz Rodríguez, J., Leenaarts, J., Danilovic, S., & Uitenbroek, H. 2019, *A&A*, 623, A74,
doi: [10.1051/0004-6361/201834464](https://doi.org/10.1051/0004-6361/201834464)

- de la Cruz Rodríguez, J., Löfdahl, M. G., Sütterlin, P., Hillberg, T., & Rouppe van der Voort, L. 2015, *A&A*, 573, A40, doi: [10.1051/0004-6361/201424319](https://doi.org/10.1051/0004-6361/201424319)
- De Pontieu, B., Title, A. M., Lemen, J. R., et al. 2014, *SoPh*, 289, 2733, doi: [10.1007/s11207-014-0485-y](https://doi.org/10.1007/s11207-014-0485-y)
- Fey, M., & Lenssen, J. E. 2019, in *ICLR Workshop on Representation Learning on Graphs and Manifolds*
- Fontenla, J. M., Avrett, E. H., & Loeser, R. 1993, *ApJ*, 406, 319
- Frutiger, C., Solanki, S. K., Fligge, M., & Bruls, J. H. M. J. 2000, *A&A*, 358, 1109
- Gudiksen, B. V., Carlsson, M., Hansteen, V. H., et al. 2011, *A&A*, 531, A154, doi: [10.1051/0004-6361/201116520](https://doi.org/10.1051/0004-6361/201116520)
- Harris, C. R., Millman, K. J., van der Walt, S. J., et al. 2020, *Nature*, 585, 357–362, doi: [10.1038/s41586-020-2649-2](https://doi.org/10.1038/s41586-020-2649-2)
- He, K., Zhang, X., Ren, S., & Sun, J. 2016, in *2016 IEEE Conference on Computer Vision and Pattern Recognition, CVPR 2016, Las Vegas, NV, USA, June 27-30, 2016*, 770–778, doi: [10.1109/CVPR.2016.90](https://doi.org/10.1109/CVPR.2016.90)
- Hubeny, I., & Mihalas, D. 2014, *Theory of stellar atmospheres: An introduction to astrophysical non-equilibrium quantitative spectroscopic analysis* (Princeton University Press)
- Hunter, J. D. 2007, *Computing in Science Engineering*, 9, 90
- Jaume Bestard, J., Trujillo Bueno, J., Štěpán, J., & del Pino Alemán, T. 2021, *ApJ*, 909, 183, doi: [10.3847/1538-4357/abd94a](https://doi.org/10.3847/1538-4357/abd94a)
- Kingma, D. P., & Ba, J. 2014, *arXiv e-prints*, arXiv:1412.6980. <https://arxiv.org/abs/1412.6980>
- Landi Degl’Innocenti, E., & Landolfi, M. 2004, *Polarization in Spectral Lines* (Kluwer Academic Publishers)
- Leenaarts, J., & Carlsson, M. 2009, in *Astronomical Society of the Pacific Conference Series*, Vol. 415, *The Second Hinode Science Meeting: Beyond Discovery-Toward Understanding*, ed. B. Lites, M. Cheung, T. Magara, J. Mariska, & K. Reeves, 87
- Löfdahl, M. G. 2002, in *Society of Photo-Optical Instrumentation Engineers (SPIE) Conference Series*, Vol. 4792, *Image Reconstruction from Incomplete Data*, ed. P. J. Bones, M. A. Fiddy, & R. P. Millane, 146–155, doi: [10.1117/12.451791](https://doi.org/10.1117/12.451791)
- Löfdahl, M. G., Hillberg, T., de la Cruz Rodríguez, J., et al. 2021, *A&A*, 653, A68, doi: [10.1051/0004-6361/202141326](https://doi.org/10.1051/0004-6361/202141326)
- Mihalas, D. 1978, in *Stellar Atmospheres*, Vol. 455
- Milić, I., & van Noort, M. 2017, *A&A*, 601, A100, doi: [10.1051/0004-6361/201629980](https://doi.org/10.1051/0004-6361/201629980)
- . 2018, *A&A*, 617, A24, doi: [10.1051/0004-6361/201833382](https://doi.org/10.1051/0004-6361/201833382)
- Osborne, C. M. J., & Milić, I. 2021, *ApJ*, 917, 14, doi: [10.3847/1538-4357/ac02be](https://doi.org/10.3847/1538-4357/ac02be)
- Paszke, A., Gross, S., Massa, F., et al. 2019, in *Advances in Neural Information Processing Systems 32*, ed. H. Wallach, H. Larochelle, A. Beygelzimer, F. d’É. Buc, E. Fox, & R. Garnett (Curran Associates, Inc.), 8024–8035. <http://shorturl.at/oDQS8>
- Pfaff, T., Fortunato, M., Sánchez-Gonzalez, A., & Battaglia, P. W. 2020, *CoRR*, abs/2010.03409
- Quintero Noda, C., Shimizu, T., de la Cruz Rodríguez, J., et al. 2016, *MNRAS*, 459, 3363, doi: [10.1093/mnras/stw867](https://doi.org/10.1093/mnras/stw867)
- Rees, D. E. 1969, *SoPh*, 10, 268, doi: [10.1007/BF00145514](https://doi.org/10.1007/BF00145514)
- Ruiz Cobo, B., & del Toro Iniesta, J. C. 1992, *ApJ*, 398, 375
- Ruiz Cobo, B., Quintero Noda, C., Gafeira, R., et al. 2021, *A&A*, in press
- Rutten, R. J. 2003, *Radiative Transfer in Stellar Atmospheres*
- Rybicki, G. B., & Hummer, D. G. 1992, *A&A*, 262, 209
- Sanchez Almeida, J. 1992, *SoPh*, 137, 1, doi: [10.1007/BF00146572](https://doi.org/10.1007/BF00146572)
- Sánchez-González, A., Godwin, J., Pfaff, T., et al. 2020, in *Proceedings of Machine Learning Research*, Vol. 119, *Proceedings of the 37th International Conference on Machine Learning, ICML 2020, 13-18 July 2020, Virtual Event (PMLR)*, 8459–8468. <http://proceedings.mlr.press/v119/sanchez-gonzalez20a.html>
- Scharmer, G. B. 2006, *A&A*, 447, 1111, doi: [10.1051/0004-6361:20052981](https://doi.org/10.1051/0004-6361:20052981)
- Scharmer, G. B., Bjelksjo, K., Korhonen, T. K., Lindberg, B., & Petterson, B. 2003, in *Proc. SPIE*, Vol. 4853, *Innovative Telescopes and Instrumentation for Solar Astrophysics*, ed. S. L. Keil & S. V. Avakyan, 341–350
- Scharmer, G. B., Narayan, G., Hillberg, T., et al. 2008, *ApJL*, 689, L69, doi: [10.1086/595744](https://doi.org/10.1086/595744)
- Socas-Navarro, H., Ruiz Cobo, B., & Trujillo Bueno, J. 1998, *ApJ*, 507, 470
- Trujillo Bueno, J., & Fabiani Bendicho, P. 1995, *ApJ*, 455, 646
- Trujillo Bueno, J., & Manso Sainz, R. 1999, *ApJ*, 516, 436
- Uitenbroek, H. 2001, *ApJ*, 557, 389
- van Noort, M., Rouppe van der Voort, L., & Löfdahl, M. G. 2005, *SoPh*, 228, 191, doi: [10.1007/s11207-005-5782-z](https://doi.org/10.1007/s11207-005-5782-z)
- Vissers, G. J. M., de la Cruz Rodríguez, J., Libbrecht, T., et al. 2019, *A&A*, 627, A101, doi: [10.1051/0004-6361/201833560](https://doi.org/10.1051/0004-6361/201833560)